

Generalization of PILE Method to the EM Scattering From Stratified Subsurface With Rough Interlayers: Application to the Detection of Debondings Within Pavement Structure

Christophe Bourlier, Cédric Le Bastard, and Vincent Baltazart

Abstract—This paper presents the numerical method, generalized propagation-inside-layer expansion (GPILE), to calculate the scattered electromagnetic field by any stratified 1-D medium composed of three random rough interfaces separating homogeneous media. GPILE is a generalization of the propagation-inside-layer expansion method, which considers only two interfaces. Both methods rely on the rigorous implementation of the Maxwell equations, with a simple matrix formulation and which have a straightforward physical interpretation. In particular, this method allows us to distinguish the primary echo of the upper surface and also the multiple echoes arising from the intermediate and lower interfaces. This method is applied in this paper to simulate the ground-penetrating radar (GPR) signal at nadir. The simulated signals are analyzed to study the sensitivity of the GPR signal to any material debonding within the pavement layered structure.

Index Terms—Debonding, electromagnetic scattering from rough layers, ground-penetrating radar (GPR), method of moments (MoM), stratified media.

I. INTRODUCTION

GROUND-penetrating radar (GPR) is a common tool for nondestructive testing of civil engineering materials (hydraulic, bituminous concretes, and soils). It allows rapid data collection and is widely used for the specific application of pavement survey [1]–[6]. Within this scope, the roadway is assumed to be horizontally stratified. The vertical structure of a roadway can then be deduced from radar-measured signal by means of echo detection and amplitude estimation. Echo detection provides time-delay estimation associated with each interface, whereas amplitude estimation is used to retrieve the wave speed (or the dielectric constant) within each layer. In the liter-

ature, electromagnetic (EM) inversion and layer stripping constitute two methods for estimating the latter parameters [4], [5].

This paper focuses on the detection and the survey of interlayer debonding within pavement structures by GPR. The debonding mechanisms have a meaningful influence on the residual life of the pavement, and thus, the early detection of the latter is an important issue for pavement maintenance [7], [8]. When undertaking pavement survey, the main difficulty with data processing relies on the echo detection of the signal backscattered from the interlayer debonding to be surveyed. To analyze the signal sensitivity to such a thin inner debonding, we propose to use a rigorous method. GPR numerical simulation is an efficient way to study and to analyze the EM wave propagation inside the considered layered medium.

The finite-difference time-domain (FDTD) method has been widely used to simulate the GPR signal, e.g., [9]–[11]. From an input time signal, it provides the simulated scattered signal from the subsurface structure. It is a full-wave method and has shown its efficiency for GPR electromagnetic problems and especially for inhomogeneous media. In this paper, we propose to use the frequency-domain numerical propagation-inside-layer expansion (PILE) [14]–[16] method to compute the scattered field by the layered medium. It is based on the well-known full-wave method of moments (MoM). The MoM meshes the boundaries (here the interfaces), whereas the FDTD meshes the space. Then, the resulting impedance matrix is sparse with FDTD, whereas it is full and of smaller size with the MoM. For rough interfaces, near the interfaces, the meshing must be refined with FDTD to well follow the surface profiles, which increases the memory space requirement, unlike the MoM. The main drawback of MoM is that it can be applied only for interfaces separated by homogeneous media and for a single frequency. Thus, to calculate a frequency response, the MoM must be applied N_f times, where N_f is the number of frequencies.

In comparison to a brute force MoM (direct LU inversion of the impedance matrix of the interfaces), the major advantage of the PILE method relies on its ability to calculate the echoes scattered by each interface with both the multiple scattering and the interlayer surface roughness accounted for. In this paper, the PILE method is generalized to M rough interfaces separated by homogeneous media. It is then applied to only three interfaces to meet the requirements of the application. As

Manuscript received July 24, 2014; revised November 25, 2014; accepted December 18, 2014.

C. Bourlier is with the Institut d'Electronique et de Télécommunications de Rennes Laboratory, LUNAM Université, Université de Nantes, 44306 Nantes Cedex, France.

C. Le Bastard is with the Institut d'Electronique et de Télécommunications de Rennes Laboratory, LUNAM Université, Université de Nantes, 44306 Nantes Cedex, France, and also with the Centre for Expertise and Engineering on Risks, Environment, Mobility, Urban and Country Planning (Cerema), DLRC Angers, 49136 Les Ponts de Cé, France.

V. Baltazart is with LUNAM Université, IFSTTAR, 44341 Bouguenais cedex, France.

Color versions of one or more of the figures in this paper are available online at <http://ieeexplore.ieee.org>.

Digital Object Identifier 10.1109/TGRS.2015.2390677

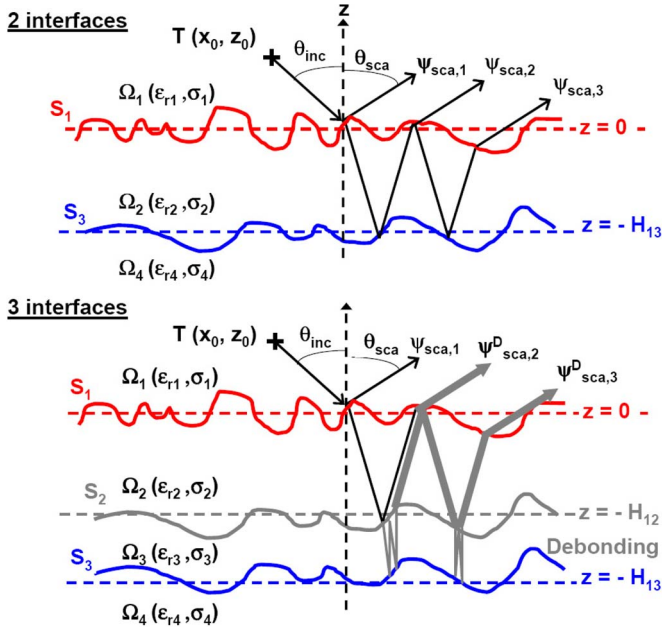


Fig. 1. (Top) Electromagnetic wave scattering from a 1-D random rough layer with two rough surfaces: representation of the first three scattered fields or echoes $\psi_{sca,1}$, $\psi_{sca,2}$, and $\psi_{sca,3}$ for an incidence angle $\theta_{inc} \neq 0$. The Cartesian coordinates of the transmitter are (x_0, z_0) . (Bottom) Electromagnetic wave scattering from 1-D three rough interfaces (pavement debonding): representation of the first three scattered fields or echoes $\psi_{sca,1}$, $\psi_{sca,2}^D$, and $\psi_{sca,3}^D$ for an incidence angle $\theta_{inc} \neq 0$.

a result, the proposed method generalization of PILE (GPIL) is expected to give further insight better understanding of the scattering phenomena in the context of interlayer debonding within pavement structures to draw some perspectives for the detection.

Section II briefly summarizes the PILE method and generalizes it to three (its generalization to M rough interfaces is addressed in the Appendix) rough interlayer interfaces. Section III presents the parameters to be used for the application and some numerical results for a single frequency. Section IV provides the simulated GPR signal over realistic scenarios of interlayer debonding within pavement structures. The sensitivity of the GPR signal to the pavement debonding is also discussed. The last section gives the concluding remarks.

II. GENERALIZATION OF THE PILE METHOD

The PILE method is able to compute the scattered field from a 1-D random rough layer made up of two random rough surfaces separating homogeneous media Ω_1 , Ω_2 , and Ω_4 (2-D problem, top of Fig. 1). An incident wave inside Ω_1 impinges upon the upper rough surface S_1 . Owing to the two surfaces, multiple scattered fields back into Ω_1 occur: not only the field $\psi_{sca,1}$ scattered by the upper rough surface S_1 (first echo) but also the higher order scattered fields (or echoes) resulting from the multiple reflections inside Ω_2 : $\psi_{sca,2}$, $\psi_{sca,3}$, and so on. The application is the GPR for nondestructive pavement survey [12], [13] by taking the roughness of the surfaces into account.

A means to geometrically feature the pavement debonding (bottom of Fig. 1) is to add an interface above the lower sur-

face S_3 . The new problem considers the scattering from three interfaces separating homogeneous media Ω_1 , Ω_2 , Ω_3 , and Ω_4 . Then, as previously, in order to calculate the contribution of each echo resulting from the multiple scattering both inside the media Ω_2 and Ω_3 , the PILE method must be generalized.

A. PILE Method

In this section, the PILE method is briefly presented from [14]–[16]. It will be applied in Section IV to simulate the GPR signal from a nonbonding layered material with two rough interfaces only, as shown at the top of Fig. 1.

From the boundary integral equations, the surface currents ψ_i and $\partial\psi_i/\partial n$ on each surface S_i ($i = \{1, 3\}$) (top of Fig. 1) must be determined. The normal derivative $\partial\psi_i/\partial n$ is defined as $\partial\psi_i/\partial n = \mathbf{n}_i \cdot \nabla\psi_i$, where $\nabla = (\partial/\partial x, \partial/\partial z)$ and $\mathbf{n}_i = (-\gamma_i, 1)/\sqrt{1 + \gamma_i^2}$ the vector normal to the surface i , with $\gamma_i = dz_i/dx$ as the slope of the surface i . From the MoM, the boundary integral equations are discretized on each surface of the scatterer, leading to the linear system $\bar{\mathbf{Z}}\mathbf{X} = \mathbf{b}$. The unknown vector is then

$$\mathbf{X} = \begin{bmatrix} \mathbf{X}_1 \\ \mathbf{X}_3 \end{bmatrix} \quad (1)$$

where the components of the vectors \mathbf{X}_1 and \mathbf{X}_3 are the surface currents discretized on the surfaces S_1 and S_3 , respectively. They are written as

$$\mathbf{X}_1 = \left[\psi_1(\mathbf{r}_1) \dots \psi_1(\mathbf{r}_{N_1}) \frac{\partial\psi_1(\mathbf{r}_1)}{\partial n} \dots \frac{\partial\psi_1(\mathbf{r}_{N_1})}{\partial n} \right]^T \quad (2)$$

where $\mathbf{r}_{p \in \{1; N_1\}} \in S_1$ and

$$\mathbf{X}_3 = \left[\psi_3(\mathbf{r}_1) \dots \psi_3(\mathbf{r}_{N_3}) \frac{\partial\psi_3(\mathbf{r}_1)}{\partial n} \dots \frac{\partial\psi_3(\mathbf{r}_{N_3})}{\partial n} \right]^T \quad (3)$$

where $\mathbf{r}_{p \in \{1; N_3\}} \in S_3$. The symbol \mathbf{T} stands for the transpose operator, and N_i is the number of samples on the surface S_i . Then, the length of the vector \mathbf{X}_i is $2N_i$.

The vector \mathbf{b} of length $2(N_1 + N_3)$ is the incident field discretized on the surface S_i . It is defined as

$$\mathbf{b} = \begin{bmatrix} \mathbf{b}_1 \\ \mathbf{b}_3 \end{bmatrix} = \left[\underbrace{\psi_{inc}(\mathbf{r}_1) \dots \psi_{inc}(\mathbf{r}_{N_1})}_{\mathbf{b}_1^T, \mathbf{r} \in S_1} \underbrace{\begin{matrix} 0 \dots 0 \\ \vdots \\ 0 \dots 0 \end{matrix}}_{N_1 \text{ times } 2N_3 \text{ times}} \underbrace{\begin{matrix} 0 \dots 0 \\ \vdots \\ 0 \dots 0 \end{matrix}}_{\mathbf{b}_3^T, \mathbf{r} \in S_3} \right]^T \quad (4)$$

The impedance matrix $\bar{\mathbf{Z}}$ of size $2(N_1 + N_3) \times 2(N_1 + N_3)$ is expressed as

$$\bar{\mathbf{Z}} = \begin{bmatrix} \bar{\mathbf{Z}}_1 & \bar{\mathbf{Z}}_{31} \\ \bar{\mathbf{Z}}_{13} & \bar{\mathbf{Z}}_3 \end{bmatrix}. \quad (5)$$

The impedance matrix $\bar{\mathbf{Z}}_i$ of size $2N_i \times 2N_i$ is the impedance matrix of a single surface i , where N_i is the number of samples on the surface i . Moreover, matrices $\bar{\mathbf{Z}}_{31}$ of size $2N_1 \times 2N_3$ (propagation from scatterer 3 to 1) and $\bar{\mathbf{Z}}_{13}$ of size $2N_3 \times 2N_1$ (propagation from surfaces 1 to 3) are coupling matrices between the two scatterers. The expressions of the elements of matrices $\bar{\mathbf{Z}}_i$ and $\bar{\mathbf{Z}}_{ij}$ ($i = \{1, 3\}$ and $j = \{1, 3\} \neq i$) can be found in [16].

To solve efficiently the system $\bar{\mathbf{Z}}\mathbf{X} = \mathbf{b}$, the PILE method has been developed [14]. It is based on the inversion by blocks (decomposition of domains from the series Taylor expansion of the inverse of the Schur complement) of the impedance matrix. This leads to

$$\mathbf{X}_1 = \left[\sum_{p=0}^{p=P_{\text{PILE}}} \bar{\mathbf{M}}_{c1}^p \right] \bar{\mathbf{Z}}_1^{-1} \mathbf{b}_1 = \sum_{p=0}^{p=P_{\text{PILE}}} \mathbf{Y}_1^{(p)} \quad (6)$$

in which

$$\begin{cases} \mathbf{Y}_1^{(0)} = \bar{\mathbf{Z}}_1^{-1} \mathbf{b}_1 & \text{for } p = 0 \\ \mathbf{Y}_1^{(p)} = \bar{\mathbf{M}}_{c1} \mathbf{Y}_1^{(p-1)} & \text{for } p > 0 \end{cases} \quad (7)$$

$$\bar{\mathbf{M}}_{c1} = \bar{\mathbf{Z}}_1^{-1} \bar{\mathbf{Z}}_{31} \bar{\mathbf{Z}}_3^{-1} \bar{\mathbf{Z}}_{13}. \quad (8)$$

In addition, $\mathbf{X}_3 = -\bar{\mathbf{Z}}_3^{-1} \bar{\mathbf{Z}}_{13} \mathbf{X}_1$. We define the norm $\|\bar{\mathbf{M}}_{c1}\|$ of a complex matrix by its spectral radius, i.e., the modulus of the eigenvalue which has the highest modulus. Expansion (6) is then valid if $\|\bar{\mathbf{M}}_{c1}\|$ is strictly smaller than 1. Equation (7) has a clear physical interpretation: The total currents on scatterer 1 are the sum of the contributions $\mathbf{Y}_1^{(p)}$ corresponding to successive iterations p . In other words, unlike a pure MoM (inversion of the impedance matrix from a direct LU algorithm), PILE can compute the scattered field inside the medium Ω_1 associated to the n th echo ($\psi_{\text{sca},n}$ in Fig. 1) expressed from $\mathbf{Y}_1^{(p)}$.

B. Generalized PILE Method: GPILE

GPILE will be applied in Section IV to simulate the GPR signal from a debonding layered material, according to the scheme depicted at the bottom of Fig. 1. This scenario requires us to generalize the PILE method to three rough interfaces. For the sake of generality, the PILE method is generalized to M rough interfaces in Appendix A, while this section presents the case for $M = 3$.

From the boundary integral equations, the surface currents ψ_i and $\partial\psi_i/\partial n$ on each surface S_i ($i = \{1, 2, 3\}$) must be determined. From the MoM, the boundary integral equations are discretized on each surface of the scatterer, leading to the linear system $\bar{\mathbf{Z}}\mathbf{X} = \mathbf{b}$. The unknown vector is then

$$\mathbf{X} = \begin{bmatrix} \mathbf{X}_1 \\ \mathbf{X}_2 \\ \mathbf{X}_3 \end{bmatrix} \quad \mathbf{b} = \begin{bmatrix} \mathbf{b}_1 \\ \mathbf{0} \\ \mathbf{0} \end{bmatrix} \quad (9)$$

and the impedance matrix $\bar{\mathbf{Z}}$ of size $2(N_1 + N_2 + N_3) \times 2(N_1 + N_2 + N_3)$ is expressed as

$$\bar{\mathbf{Z}} = \begin{bmatrix} \bar{\mathbf{Z}}_1 & \bar{\mathbf{Z}}_{21} & \bar{\mathbf{0}} \\ \bar{\mathbf{Z}}_{12} & \bar{\mathbf{Z}}_2 & \bar{\mathbf{Z}}_{32} \\ \bar{\mathbf{0}} & \bar{\mathbf{Z}}_{23} & \bar{\mathbf{Z}}_3 \end{bmatrix}. \quad (10)$$

In addition

$$\mathbf{X}_i = \left[\psi_i(\mathbf{r}_1) \dots \psi_i(\mathbf{r}_{N_i}) \frac{\partial\psi_i(\mathbf{r}_1)}{\partial n} \dots \frac{\partial\psi_i(\mathbf{r}_{N_i})}{\partial n} \right]^T \quad (11)$$

where $\mathbf{r}_{p \in [1; N_i]} \in S_i$.

We can note that the coupling matrices $\bar{\mathbf{Z}}_{31}$ and $\bar{\mathbf{Z}}_{13}$ vanish because there is no direct interaction between interfaces S_1 and S_3 . It is important to note that, if the surface S_2 is replaced by an object (closed surface), then the previous matrices do not vanish because the object can interact both with the surfaces S_1 (matrices $\bar{\mathbf{Z}}_{21}$ and $\bar{\mathbf{Z}}_{12}$) and S_3 (matrices $\bar{\mathbf{Z}}_{31}$ and $\bar{\mathbf{Z}}_{13}$).

The addition of the interface S_2 can modify the field $\psi_{\text{sca},p}$ ($p > 1$) of each echo coming from the rough layer composed of only two surfaces S_1 and S_3 (no debonding). Then, to quantify this variation defined as $\psi_{\text{sca},p}^D - \psi_{\text{sca},p}$ (superscript "D" for debonding), the PILE method is generalized.

Comparing (5) and (10), (8) remains valid with the following changes:

$$\bar{\mathbf{Z}}_{31} \rightarrow \bar{\mathbf{P}}_{21} = \begin{bmatrix} \bar{\mathbf{Z}}_{21} & \mathbf{0} \end{bmatrix}_{(2N_1) \times (2N_2 + 2N_3)} \quad (12)$$

$$\bar{\mathbf{Z}}_{13} \rightarrow \bar{\mathbf{P}}_{12} = \begin{bmatrix} \bar{\mathbf{Z}}_{12} \\ \mathbf{0} \end{bmatrix}_{(2N_2 + 2N_3) \times (2N_1)} \quad (13)$$

$$\bar{\mathbf{Z}}_3 \rightarrow \bar{\mathbf{P}} = \begin{bmatrix} \bar{\mathbf{Z}}_2 & \bar{\mathbf{Z}}_{32} \\ \bar{\mathbf{Z}}_{23} & \bar{\mathbf{Z}}_3 \end{bmatrix}_{(2N_2 + 2N_3) \times (2N_2 + 2N_3)} \quad (14)$$

and then

$$\begin{cases} \bar{\mathbf{M}}_{c1} = \bar{\mathbf{Z}}_1^{-1} \bar{\mathbf{P}}_{21} \bar{\mathbf{P}}^{-1} \bar{\mathbf{P}}_{12} = \bar{\mathbf{Z}}_1^{-1} \bar{\mathbf{Z}}_{21} \bar{\mathbf{P}}_2^{-1} \bar{\mathbf{Z}}_{12} \\ \mathbf{X}_2 = -\bar{\mathbf{P}}^{-1} \bar{\mathbf{P}}_{12} \mathbf{X}_1 = -\bar{\mathbf{P}}_2^{-1} \bar{\mathbf{Z}}_{12} \mathbf{X}_1 \end{cases} \quad (15)$$

where $\bar{\mathbf{P}}_2^{-1}$ is a matrix of size $2N_2 \times 2N_2$ of elements equal to the elements of the inverse matrix $\bar{\mathbf{P}}$ by taking only the first $2N_2$ rows and columns.

Then, from (15) and (7), we must compute $\bar{\mathbf{P}}_2^{-1} \bar{\mathbf{Z}}_{12} \mathbf{Y}_1^{(p-1)} = \bar{\mathbf{P}}_2^{-1} \mathbf{v}_2$, where $\mathbf{v}_2 = \bar{\mathbf{Z}}_{12} \mathbf{Y}_1^{(p-1)}$. Then, the use of the PILE method leads to

$$\bar{\mathbf{P}}_2^{-1} \bar{\mathbf{Z}}_{12} \mathbf{Y}_1^{(p-1)} = \sum_{q=0}^{q=Q_{\text{PILE}}} \mathbf{Y}_2^{(q)} \quad (16)$$

in which

$$\begin{cases} \mathbf{Y}_2^{(0)} = \bar{\mathbf{Z}}_2^{-1} \mathbf{v}_2 & \text{for } q = 0 \\ \mathbf{Y}_2^{(q)} = \bar{\mathbf{M}}_{c2} \mathbf{Y}_2^{(q-1)} & \text{for } q > 0 \\ \bar{\mathbf{M}}_{c2} = \bar{\mathbf{Z}}_2^{-1} \bar{\mathbf{Z}}_{32} \bar{\mathbf{Z}}_3^{-1} \bar{\mathbf{Z}}_{23} \end{cases} \quad (17)$$

and $\mathbf{X}_3 = -\bar{\mathbf{Z}}_3^{-1} \bar{\mathbf{Z}}_{23} \mathbf{X}_2$.

In conclusion, the currents \mathbf{X}_1 are given by (6), in which $\mathbf{Y}_1^{(p)}$ is expressed for $p > 0$ as

$$\mathbf{Y}_1^{(p)} = \bar{\mathbf{Z}}_1^{-1} \bar{\mathbf{Z}}_{21} \sum_{q=0}^{q=Q_{\text{PILE}}} \mathbf{Y}_2^{(q)}. \quad (18)$$

Thus, the main steps of the GPILE algorithm are the following.

- 1) The contribution of the first echo $\psi_{\text{sca},1}$ is computed from $\bar{\mathbf{Z}}_1^{-1} \mathbf{b}_1 = \mathbf{Y}_1^{(0)}$, corresponding to the current at the zeroth order (surfaces S_2 and S_3 do no interact) on the surface S_1 .

- 2) On the surface S_2 , the currents at the zeroth order $\mathbf{X}_2^{(0)} = \sum_q \mathbf{Y}_2^{(q)}$, resulting from the multiple scattering inside Ω_3 , are computed from (16) from $\mathbf{v}_2 = \bar{\mathbf{Z}}_{12} \mathbf{Y}_1^{(0)}$.
- 3) On the surface S_1 , the currents at the first order $\mathbf{Y}_1^{(1)}$, resulting from the multiple scattering both inside Ω_2 and Ω_3 , are computed from (18) with $\sum_q \mathbf{Y}_2^{(q)} = \mathbf{X}_2^{(0)}$. It gives the contribution of the second echo $\psi_{sca,2}^D$.
- 4) On the surface S_2 , the currents at the first order $\mathbf{X}_2^{(1)} = \sum_q \mathbf{Y}_2^{(q)}$, resulting from the multiple scattering inside Ω_3 , are computed from (16) with $\mathbf{v}_2 = \bar{\mathbf{Z}}_{12} \mathbf{Y}_1^{(1)}$.
- 5) On the surface S_1 , the currents at the second order $\mathbf{Y}_1^{(2)}$, resulting from the multiple scattering both inside Ω_2 and Ω_3 , are computed from (18) with $\sum_q \mathbf{Y}_2^{(q)} = \mathbf{X}_2^{(1)}$. It gives the contribution of the third echo $\psi_{sca,3}^D$.
- 6) And so on for the next orders.

The currents on the surface S_3 at the order p are computed from $\mathbf{X}_3^{(p)} = -\bar{\mathbf{Z}}_3^{-1} \bar{\mathbf{Z}}_{23} \mathbf{X}_2^{(p)}$.

Physically, the order P_{PILE} corresponds to the number of back-and-forth between S_1 and S_2 which contributes to the scattering process. Typically, for an application to GPR for nondestructive pavement survey, $P_{\text{PILE}} = 1$ [13], which means that only the first two echoes contribute (scenario at the top of Fig. 1). The order Q_{PILE} corresponds to the number of back-and-forth between S_2 and S_3 which contributes to the scattering process. Its value will be determined.

GPILE is also able to calculate the contributions of all echoes arising both from S_1 , S_2 , and S_3 . For example, the sum of the i th primary (first interaction with the surface S_i) echo can be obtained for $\{P_{\text{PILE}} = 0, Q_{\text{PILE}} = 0\}$, $\{P_{\text{PILE}} = 1, Q_{\text{PILE}} = 0\}$, and $\{P_{\text{PILE}} = 1, Q_{\text{PILE}} = 1\}$, respectively, with $i = \{1, 2, 3\}$. By making the difference between them, the contribution of each i th primary echo can be retrieved.

If the size of the matrix $\bar{\mathbf{Z}}$ defined by (10) does not exceed 11 000, a direct LU inversion can be applied to invert $\bar{\mathbf{Z}}$. Then, the currents on S_1 result from the multiple echoes, and then, it is not possible to have the contribution of each echo. This inversion will be used to determine the orders P_{PILE} and Q_{PILE} .

Another advantage of GPILE is that any fast method developed for a single interface can be applied to decrease the computing time and/or the memory requirement. Here, this way is not required because the number of unknowns $2(N_1 + N_2 + N_3)$ does not exceed 11 000.

Appendix A presents the generalization of PILE to M interfaces separating homogeneous media.

III. NUMERICAL RESULTS FOR A SINGLE FREQUENCY

The simulation parameters are chosen to match to the conventional GPR configuration used for pavement survey at traffic speed (e.g., [17] and [18]), i.e., air-coupled radar configuration at vertical incidence (nadir, $\theta_{\text{inc}} = 0$ in Fig. 1). It is assumed that the scope of the probing is limited to the first two layers of the multilayer pavement structure. For no debonding pavement,

TABLE I
VALUES OF THE PERMITTIVITIES, CONDUCTIVITIES, THICKNESSES, HEIGHT SURFACE RMSs, SURFACE HEIGHT CORRELATION LENGTHS, SURFACE LENGTHS, ANTENNA PARAMETERS, AND NUMBER OF POINTS PER WAVELENGTH $\lambda_0 = c/f$ (DEFINED IN VACUUM) ON EACH SURFACE

Permittivities	$\{\epsilon_{r,2}, \epsilon_{r,3}, \epsilon_{r,4}\}$	(4.5, 3, 7)
Conductivities [S/m]	$\{\sigma_2, \sigma_3, \sigma_4\}$	$(10^{-3}, 10^{-2}, 5 \times 10^{-3})$
Thicknesses [mm]	$\{H_{12}, H_{13}\}$	(50, 60)
RMSs heights [mm]	$\{\sigma_{z,1}, \sigma_{z,2}, \sigma_{z,3}\}$	(1, 3, 2)
Correlation lengths [mm]	$\{L_{c,1}, L_{c,2}, L_{c,3}\}$	(10, 30, 30)
Surface lengths	$\{L_1, L_2, L_3\}$ [mm]	(3000, 3000, 3000)
Emitter coordinates	$\{z_0, x_0, \theta_0\}$	(470 mm, 0, 60°)
Number of samples	$\{n_1, n_2, n_3\}$	(20, 20, 20)

this corresponds to the two rough surfaces represented at the top of Fig. 1.

The pavement under study is structured into two overlying layers, i.e., the wearing course Ω_2 with mean thickness $H_{13} = 60$ mm and the base layer Ω_4 which is assumed to be semi-infinite in depth. Both layers are assumed to be equivalent to homogeneous media at normal incidence and over the GPR frequency bandwidth. Their relative permittivities $\epsilon_{r,i}$ ($i = \{2, 4\}$) typically range between 4 and 8, and their conductivities σ are between 10^{-3} and 10^{-2} S/m. To simulate a debonding within the pavement structure, the rough interface S_2 is inserted between S_1 and S_3 ; the permittivity of the medium Ω_3 is chosen to be lower than that of Ω_2 . The parameter values are reported in Table I.

Then, by considering nondispersive media, the complex relative permittivity $\epsilon_{r,i}(f)$ of the medium Ω_i ($i \in \{2, 3, 4\}$) can be calculated as

$$\epsilon_{r,i}(f) = \epsilon_{r,i} + j \frac{\sigma_i}{2\pi f \epsilon_0} \quad (19)$$

with $\epsilon_0 = 1/(36\pi 10^9)$ F/m as the permittivity inside the vacuum. The medium Ω_1 is assumed to be vacuum.

The three rough interfaces S_1 , S_2 , and S_3 are assumed to have a Gaussian height probability density function. Surfaces S_1 and S_3 are considered as uncorrelated, while surfaces S_2 and S_3 are correlated. About the surface height autocorrelation function (ACF), some studies [19], [20] showed that it is closer to an exponential function than a Gaussian one. Then, it is interesting to look at the influence of the choice of the correlation on the scattered field. Gaussian and exponential ACFs are defined as

$$\begin{cases} C_z(x) = \sigma_z^2 \exp\left(-\frac{x^2}{L_c^2}\right) \\ C_z(x) = \sigma_z^2 \exp\left(-\frac{|x|}{L_c}\right) \end{cases} \quad (20)$$

and the corresponding spectra (or power density function), defined as the Fourier transform of C_z , are

$$\begin{cases} \hat{C}_z(k) = \sigma_z^2 L_c \sqrt{\pi} \exp\left(-\frac{k^2 L_c^2}{4}\right) \\ \hat{C}_z(k) = \frac{2\sigma_z^2 L_c}{1+k^2 L_c^2} \end{cases} \quad (21)$$

where L_c is the surface height correlation length and σ_z is the surface root-mean-square (rms) height. The random surface

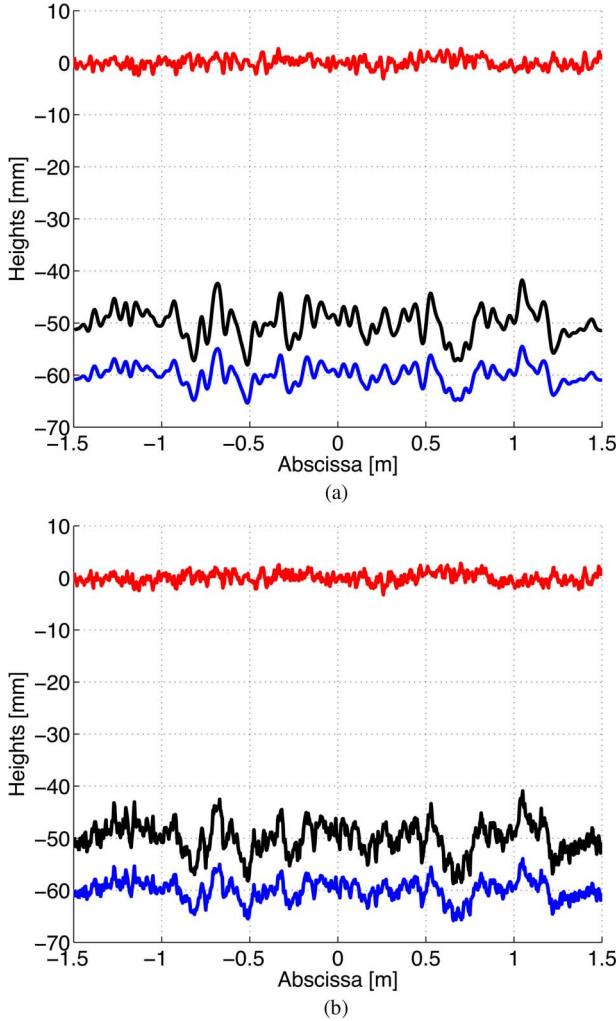


Fig. 2. Surface heights versus their abscissa for the Gaussian (top) and exponential (bottom) ACFs. The values $L_{c,i}$ and $\sigma_{z,i}$ ($i = \{1, 2, 3\}$) are reported in Table I. (a) Gaussian ACF. (b) Exponential ACF.

profiles are generated from the method of chapter 1 of [16]. For the three surfaces $i = \{1, 2, 3\}$, the values of $L_{c,i}$ and $\sigma_{z,i}$ are reported in Table I.

In what follows, the symbol $\hat{\cdot}$ means that the variable is expressed in the frequency domain.

Fig. 2 plots the surface heights versus their abscissa for the Gaussian (top) and exponential (bottom) ACFs. As we can see, surfaces with an exponential ACF are more irregular than those obtained with a Gaussian ACF due to the high-frequency components, which contribute, unlike for a Gaussian ACF (see (21) for $kL_c > 1$). In this paper, we consider only one realization of the surfaces.

The antenna is assumed to radiate a vertically polarized plane wave in the far field of the probed pavement: the antenna is about 470 mm (phase center) above the upper surface S_1 , for which the far-field condition has been checked for the antenna (not for the scattered field because the upper surface length is much larger than the size of the antenna). The angular width (at -3 dB, θ_0) of the antenna depends on the frequency and is ranged from 45° to 90° . Here, we use $\theta_0 = 60^\circ$, and it is assumed to be a constant. The Thorsos beam is used to model

the incident field radiated by the antenna. It is a tapered plane wave, whose tapering has a Gaussian shape; the tapering is used to reduce the incident field to near zero at the ends of the surfaces and thereby to reduce edge effects to negligible levels. For a normal ($\theta_{\text{inc}} = 0$) incident wave, on the surface, its modulus is equal to $e^{-x_1^2/g^2}$ (x_1 abscissa of the surface S_1 centered on zero), where g controls the attenuation on the surface. Then, from θ_0 , the surface length $L_0 = 2z_0 \tan(\theta_0/2) = 0.39$ m, for which the incident power at the extremities of the surface is -3 dB. Then, $g = L_0 \sqrt{20/(3 \ln 10)} = 0.66$ m. To reduce the edge effects, the lengths of the three surfaces are then $L_i = 3$ m $\approx 5g$. The MoM with a classical LU inversion (it is similar to considering an infinite number of echoes) is used to check the convergence of GPiLE.

Fig. 3 plots the modulus of the scattered field in decibel scale, $20 \log_{10} |\hat{\psi}_{\text{sca}}|$, versus the observation abscissa $x_{\text{obs}} \in [-L_1/2; L_1/2]$ and for an observation height $z_{\text{obs}} = z_0 = 470$ mm. The frequency is $f = f_0 = 4$ GHz, the surfaces have a Gaussian ACF, and $Q_{\text{PILE}} = 4$. The number of points n_i ($i = \{1, 2, 3\}$) per wavelength $\lambda_0 = c/f = 7.5$ cm ($c \approx 3 \times 10^8$ m/s) is reported in Table I. Then, the number of unknowns is 4800. In the legend, the number is the relative residual error (RRE), $\hat{\epsilon}_{\text{sca}, P_{\text{PILE}}}$ at the order P_{PILE} , between the scattered field $\hat{\psi}_{\text{sca}}$ computed from the selected method (PILE or GPiLE) and that computed from a direct LU inversion $\hat{\psi}_{\text{sca}, \text{LU}}$ (by considering the pavement debonding), defined as

$$\hat{\epsilon}_{\text{sca}, P_{\text{PILE}}} = \frac{\text{norm}(\hat{\psi}_{\text{sca}, P_{\text{PILE}}} - \hat{\psi}_{\text{sca}, \text{LU}})}{\text{norm}(\hat{\psi}_{\text{sca}, \text{LU}})} \quad (22)$$

where norm is the L_2 norm, computed over $x_{\text{obs}} \in [-L_1/2; L_1/2]$. For PILE (no pavement debonding), the order P_{PILE} is given in the legend of the panels, and for GPiLE (pavement debonding), the orders P_{PILE} and Q_{PILE} are given in the legend of the panels ($P_{\text{PILE}}/Q_{\text{PILE}}$).

As we can see in Fig. 3(a), the incident field on the surface decreases as $|x_1|$ increases to avoid the edge diffraction phenomenon. In Fig. 3(b), PILE and GPiLE at the order $P_{\text{PILE}} = 0$ compute the field scattered by the only upper surface S_1 (echo 1), which explains why the scattered fields are equal. In Fig. 3(c) for $P_{\text{PILE}} = 1$, the scattered fields differ because, for PILE, the surfaces S_1 interact only with S_2 , whereas for GPiLE, the surfaces S_1 interact with S_3 via S_2 . Then, the pavement debonding modified the scattered field. In Fig. 3(d), the scattered field computed from a direct LU inversion (all echoes) matches that obtained from GPiLE, which means that only the first three ($P_{\text{PILE}} + 1$) echoes contribute to the scattering process.

Fig. 4 plots the ratio $|\hat{\psi}_{\text{sca}, \text{GPiLE}}/\hat{\psi}_{\text{sca}, \text{LU}}|$ in decibel scale (difference $|\hat{\psi}_{\text{sca}, \text{GPiLE}}|_{\text{dB}} - |\hat{\psi}_{\text{sca}, \text{LU}}|_{\text{dB}}$) versus the observation abscissa $x_{\text{obs}} \in [-L_1/2; L_1/2]$ and for an observation height $z_{\text{obs}} = z_0 = 470$ mm. The frequency is $f = f_0 = 4$ GHz, and the surfaces have a Gaussian ACF. The order $P_{\text{PILE}} = 2$ (first three echoes), and Q_{PILE} varies. As Q_{PILE} increases, the mean ratio decreases, and for $Q_{\text{PILE}} = 3$, the convergence is reached. Then, $Q_{\text{PILE}} = 3$, which means that three back-and-forth between the surfaces S_2 and S_3 are required.

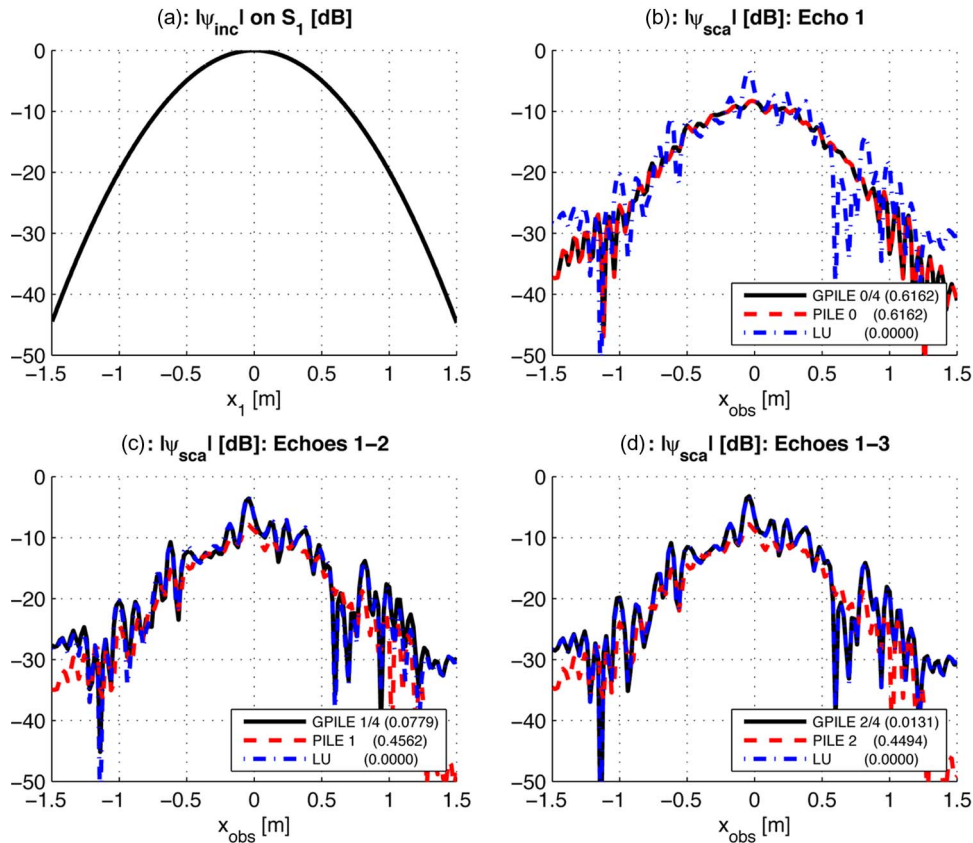


Fig. 3. (a) Modulus of the incident field on the surface in decibel scale ($20 \log_{10} |\hat{\psi}_{inc}|$) versus the surface abscissa x_1 of S_1 . (b)–(d) Modulus of the scattered field in decibel scale ($20 \log_{10} |\hat{\psi}_{sca}|$) versus the observation abscissa $x_{obs} \in [-L/2; L/2]$ and for an observation height $z_{obs} = z_0 = 470$ mm. The frequency is $f = f_0 = 4$ GHz, the surfaces have a Gaussian ACF, and $Q_{PILE} = 4$.

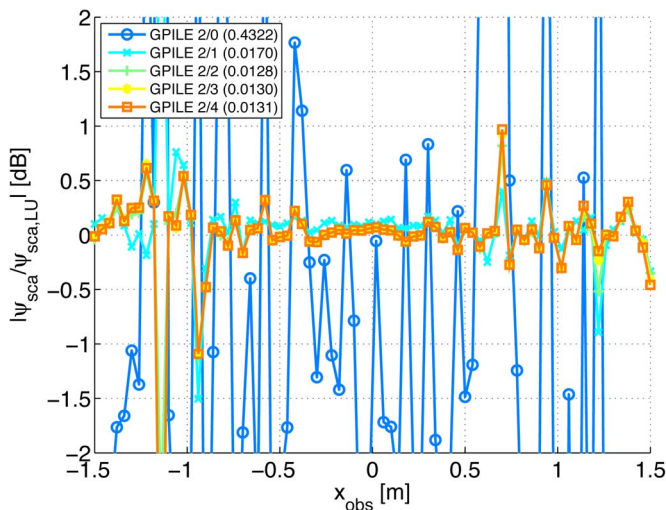


Fig. 4. Ratio $|\hat{\psi}_{sca,GPILE}|/|\hat{\psi}_{sca,LU}|$ in decibel scale (difference $|\hat{\psi}_{sca,GPILE}|_{dB} - |\hat{\psi}_{sca,LU}|_{dB}$) versus the observation abscissa $x_{obs} \in [-L_1/2; L_1/2]$ and for an observation height $z_{obs} = z_0 = 470$ mm. The frequency is $f = f_0 = 4$ GHz, and the surfaces have a Gaussian ACF. The order $P_{PILE} = 2$ (first three echoes), and Q_{PILE} varies.

In the next section, the reception antenna is located at $x_{obs} = x_0 + 20 = 20$ cm, and its height is $z_{obs} = z_0$. Then, with $P_{PILE} = 3$ and $Q_{PILE} = 3$, the error with LU does not exceed 0.1 dB.

Fig. 5 plots the same variations as in Fig. 3(d), but the three surfaces are uncorrelated, and $H_{12} = 45$ mm (the thickness is

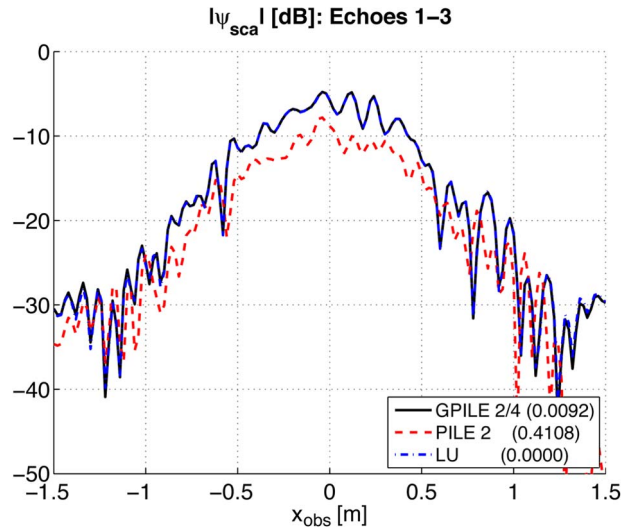


Fig. 5. Same variations as in Fig. 3(d) but the three surfaces are uncorrelated and $H_{12} = 45$ mm.

smaller to avoid the intersection of the surface S_2 with S_3). Fig. 6 plots the same variations as in Fig. 3(d), but the three surfaces have an exponential ACF. Figs. 5 and 6 show a very good agreement between GPILE and LU. Other simulations, not plotted here, also showed that the GPILE results matched with those of LU whatever the surface correlation lengths and the rms heights.

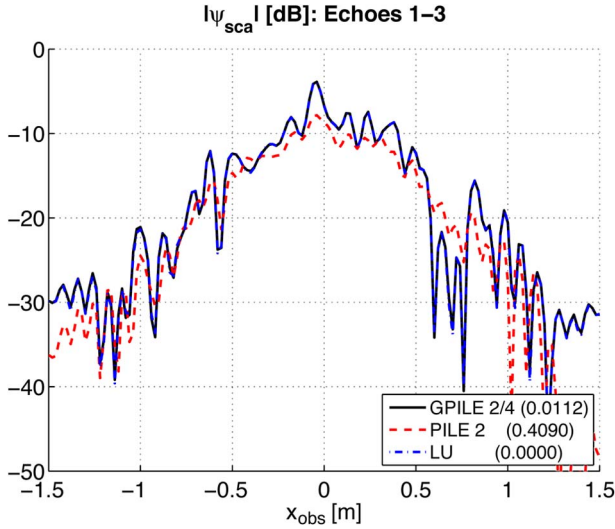


Fig. 6. Same variations as in Fig. 3(d) but the three surfaces have an exponential ACF.

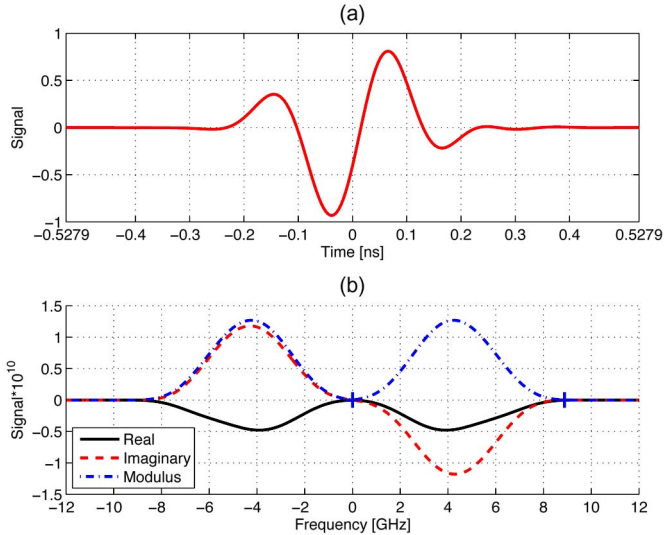


Fig. 7. (a) Signal versus the time t . (b) Its Fourier transform versus the frequency f .

IV. GPR DATA SIMULATION

In this section, the PILE and GPILE methods are used to provide simulated GPR data on healthy and debonding pavement structures, respectively, according to the scheme depicted in Fig. 1. To compute the GPR response, either PILE or GPILE is performed on the N_f equally spaced frequencies covering the GPR bandwidth. The number of points n_i ($i = \{1, 2, 3\}$) per wavelength $\lambda_{0,\min} = 3.34$ cm ($c \approx 3 \times 10^8$ m/s) on the surface S_i is reported in Table I. Then, the total number of unknowns is 10788. For a given frequency, the computing time for GPILE is on the order of 60 s.

In this paper, the realistic GPR pulse shown in Fig. 7 $s(t)$ is considered as an input. Also, this figure plots its Fourier transform $\hat{s}(f)$, which is required to determine the amplitude of the incident field for a given frequency to run the GPILE method. The number of time samples of s is $N_s = 1281$, and the time $t \in [-0.5279; 0.5279]$ ns. To have a better resolution in the frequency domain, the zero-padding technique is applied

to increase N_s to $2^{15} = 32768$. Then, the sampling step in the frequency domain is $\Delta f = 0.037$ GHz. As shown in Fig. 7(b), the signal is Hermitian, i.e., $\hat{s}(-f)^* = \hat{s}(f)$, where the symbol $*$ stands for the complex conjugate.

For the computation of the scattered field, only the positive frequencies for which $|\hat{s}(f)| \geq 10^{-3}$ are selected. Then, $N_f = 244$ with $f_{\min} = 0.0370$ GHz and $f_{\max} = 8.991$ GHz. For $|f| \notin [f_{\min}; f_{\max}]$, the scattered field $\hat{\psi}_{sca}$ is set to zero. In addition, for the negative frequencies, $\hat{\psi}_{sca}(-f) = \hat{\psi}_{sca}(f)^*$. Then, from an IFFT, the corresponding time signal ψ_{sca} of the scattered field is computed.

Fig. 8 plots the frequency responses $|\hat{s}_{sca}|$ of the modulus of the scattered field versus the frequency f . $z_{\text{obs}} = z_0 = 470$ mm, $x_{\text{obs}} = 20$ cm, and the surfaces have a Gaussian ACF. For Fig. 8(b)–(d), the RRE defined from (22) is given between parenthesis. Fig. 8(a) shows that the scattered field is strongly modified in comparison to the input signal, and a very good agreement is obtained between LU (all echoes) and GPILE (first three echoes; see also Fig. 8(d) for the RRE). Fig. 8(b) shows that PILE and GPILE give the same results because the incident wave interacts only with the upper surface S_1 . On the other hand, in Fig. 8(c), the results differ strongly because the incident wave interacts with S_1 and S_2 (no pavement debonding) for PILE, whereas the incident wave interacts with S_1 and S_3 via S_2 for GPILE.

Fig. 9(a) plots the time responses s_{sca} of the scattered field. The parameters are the same as in Fig. 8. The time origin t_0 is defined as the first maximum of $s(t)$, i.e., first positive break of the signal. For the no debonding case and smooth interfaces, the first, second, and third echoes arise from the times $t_1, t_2,$ and t_3 defined as

$$\begin{cases} t_1 = t_0 + 2(z_0 + z_{\text{obs}})/c \\ t_2 = t_1 + 2H_{13}\text{Re}(\sqrt{\epsilon_{r,2}})/c \\ t_3 = t_2 + 2H_{13}\text{Re}(\sqrt{\epsilon_{r,2}})/c. \end{cases} \quad (23)$$

As shown in Fig. 1, for the debonding case, it is important to note that the second and third echoes result from the scattering from the interface S_2 and the multiple scattering inside Ω_3 , implying that the echoes are received over a larger range time. Assuming that only one back-and-forth ($Q_{\text{PILE}} \approx 1$ from Fig. 4 at $x_{\text{obs}} = 20$ cm) contributes in the medium Ω_3 , the first three echoes are (superscript “D” for debonding)

$$\begin{cases} t_1^D = t_1 \\ \Delta t_2^D \in [t_2^D = t_1 + \tau_1; t_{20} = t_2^D + \tau_2] \\ \Delta t_3^D \in [t_3^D = t_{20} + \tau_1; t_{30} = t_2^D + \tau_2] \end{cases} \quad (24)$$

where $\tau_1 = 2H_{12}\text{Re}(\sqrt{\epsilon_{r,2}})/c$ and $\tau_2 = 2(H_{13} - H_{12})\text{Re}(\sqrt{\epsilon_{r,3}})/c$.

Fig. 9(b)–(d) plots the time responses s_{sca} of the scattered field of the first, second, and third echoes, respectively. In addition, for Fig. 9(b), the time response of a smooth surface $a_1 * s(t - t_1)$ is plotted, where a_1 is obtained from the Fresnel reflexion coefficient. Fig. 10 plots the envelop (defined as the magnitude of the Hilbert transform; it enables us to distinguish the energy peaks associated to each contribution) of the time responses s_{sca} of the scattered field of the first, second, and

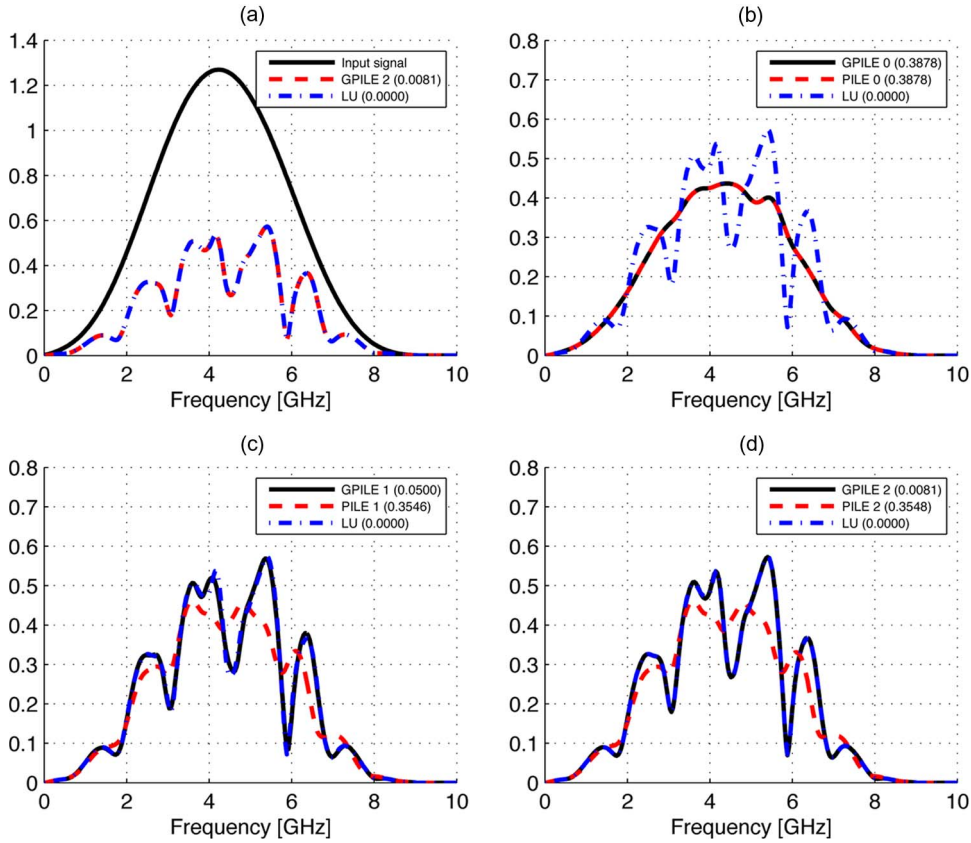


Fig. 8. Frequency responses $|\hat{s}_{sca}|$ of the modulus of the scattered field. $P_{PILE} = 3$, $z_{obs} = z_0 = 470$ mm, $x_{obs} = 20$ cm, and the surfaces have a Gaussian ACF. (a) All echoes. (b) Echoes 1–1. (c) Echoes 1–2. (d) Echoes 1–3.

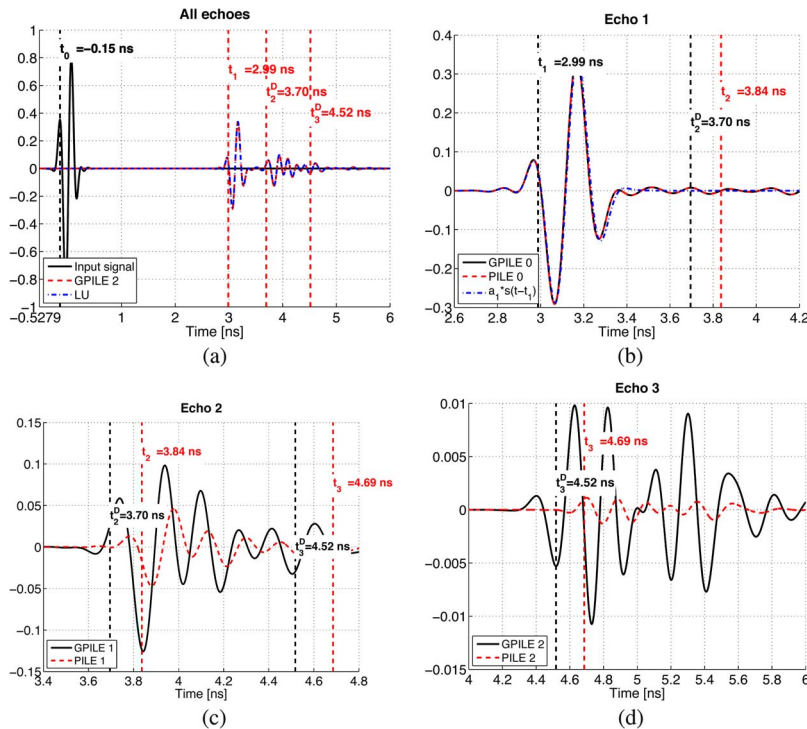


Fig. 9. (a) Time response s_{sca} of the scattered field. (b) Time response of the first echo. (c) Time response of the second echo. (d) Time response of the third echo. The parameters are the same as in Fig. 8.

third echoes, respectively, but only for GPILE and comparison between rough and smooth interfaces. The simulation parameters are the same as in Fig. 9.

As we can see in Fig. 9(a) and (b), the first echo is strongly correlated to the input signal, whereas for the second and third echoes, the input signal is strongly modified. As the order

P_{PILE} increases, the amplitude of the echoes decreases significantly (approximately divided by 10 between two successive echoes). The times given from (23) and (24) are in agreement with the observations.

In Fig. 9(c), for the second echo, PILE shows the influence of the interlayer roughness only, i.e., S_3 , while GPILE takes account for the multiple interactions between the interfaces S_2 and S_3 . From the PILE results, the roughness produces a larger time duration of the echo [see also Fig. 10(b)], about twice the initial time duration of the transmitter pulse at least. Moreover, the echo exhibits three energy peaks. The first magnitude peak over the time range [3.6; 4.1] ns represents the leading part of the transmitter pulse, which is shifted in time as it would be from a smooth interface. The roughness produces a second overlapping energy peak over the range time [4.1; 4.4] ns; this echo is then scattered two times between the interfaces S_1 and S_3 to provide the energy peak on the time range [4.4; 4.8] ns. For the debonding case, the second echo has the same overall shape as that for the nonbonding case. However, the echo is shifted at earlier time because of the smaller thickness (the debonding is located above the interface S_3) of the first layer. The amplitude of the echo is enhanced because of the constructive interferences between the scattered field by both interfaces S_2 and S_3 for the selected debonding thickness. In addition, the echo is spread over a larger time duration compared to the nonbonding case.

In Fig. 9(d), for the third echo as for the second echo in Fig. 9(c), GPILE provides a stronger amplitude because of the constructive interferences between the echo scattered by the interfaces S_2 and S_3 . The multiple scattering strongly modified the signal shape of the initial transmitter pulse. In Fig. 10(c), two magnitude peaks are shown over the time ranges [4.4; 5] and [5.1; 5.6] ns, respectively. The relative magnitude of the second peak with respect to the first one would depend on both the dielectric contrast between the interfaces and the interface roughness [see also Fig. 10(c)].

Fig. 10 clearly shows that the roughness produces degenerated (main echoes are divided into subechoes) echoes and increases the time duration of the echoes.

Fig. 11 plots the frequency responses \hat{s}_{sca} of the scattered field computed from GPILE. The parameters are the same as in Fig. 8, and the results obtained from an exponential ACF are also plotted. In the legend, they are labeled by the letter ‘‘E’’, whereas the results for a Gaussian ACF are labeled by the letter ‘‘G.’’ Fig. 11(b)–(d) plots the frequency responses of *each* echo. Fig. 12 plots the corresponding time responses s_{sca} .

Fig. 12(b) and (c) shows that the first two echoes are less sensitive to the ACF, unlike the third echo plotted in Fig. 12(d). In addition, for lower frequencies, the results are independent of the ACF because the surfaces can be considered as smooth. In comparison to a Gaussian ACF, the levels of the second and third echoes are smaller because the EM field is scattered within a larger beamwidth than that obtained with a Gaussian ACF. Indeed, with an exponential ACF, the surfaces are more irregular due to their high-frequency components. Fig. 12(c) and (d) also shows that the positions of the extrema do not move significantly with the ACF.

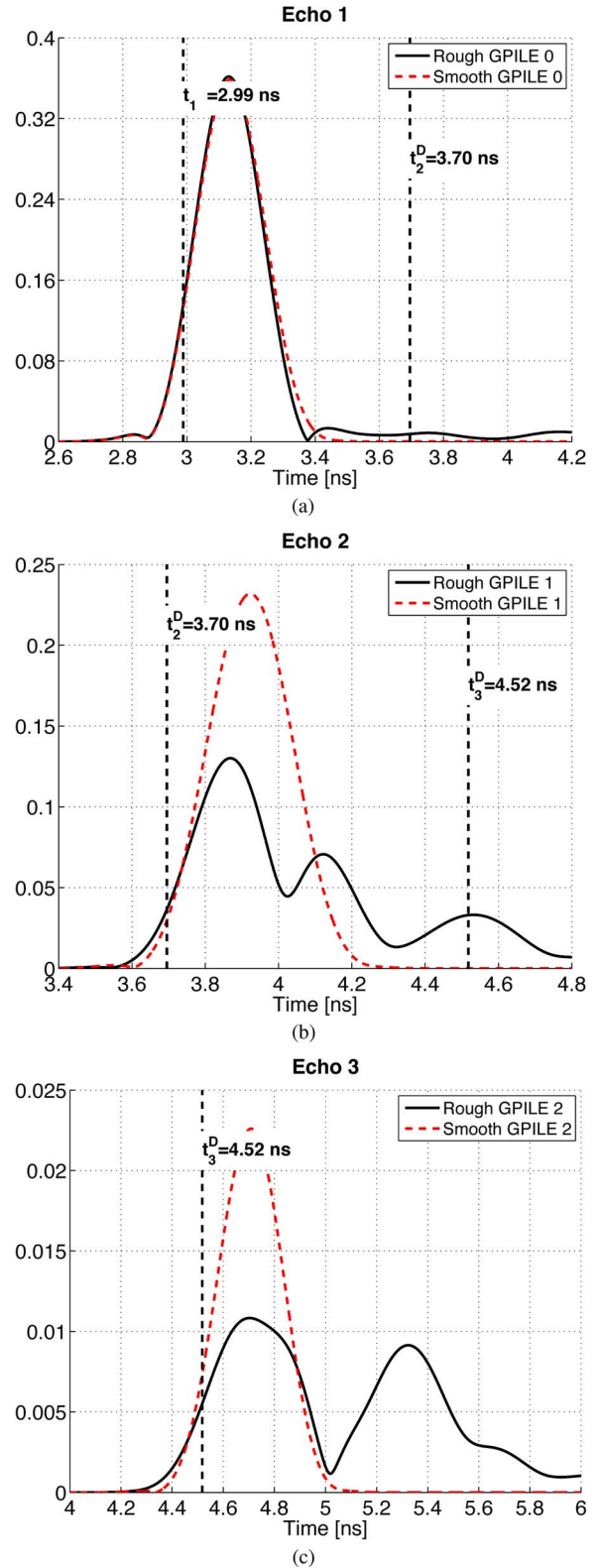


Fig. 10. Envelop (defined as the magnitude of the Hilbert transform) of the time responses s_{sca} of the scattered field of the first, second, and third echoes, respectively, but only for GPILE and comparison between rough and smooth interfaces. The same parameters as is Fig. 9.

V. CONCLUSION

In this paper, the GPILE method has been developed to rigorously solve the EM scattering by a stratified medium

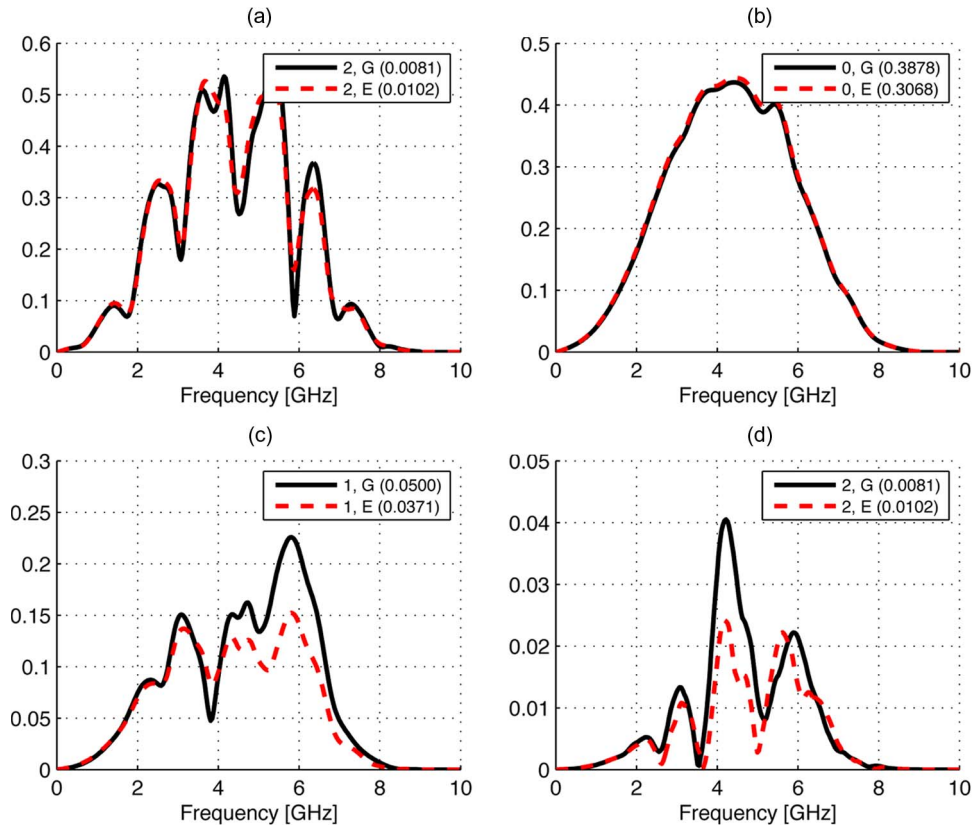


Fig. 11. Frequency responses \hat{s}_{sca} of the scattered field computed from GPILE. The parameters are the same as in Fig. 8, and the results obtained from an exponential ACF are also plotted.

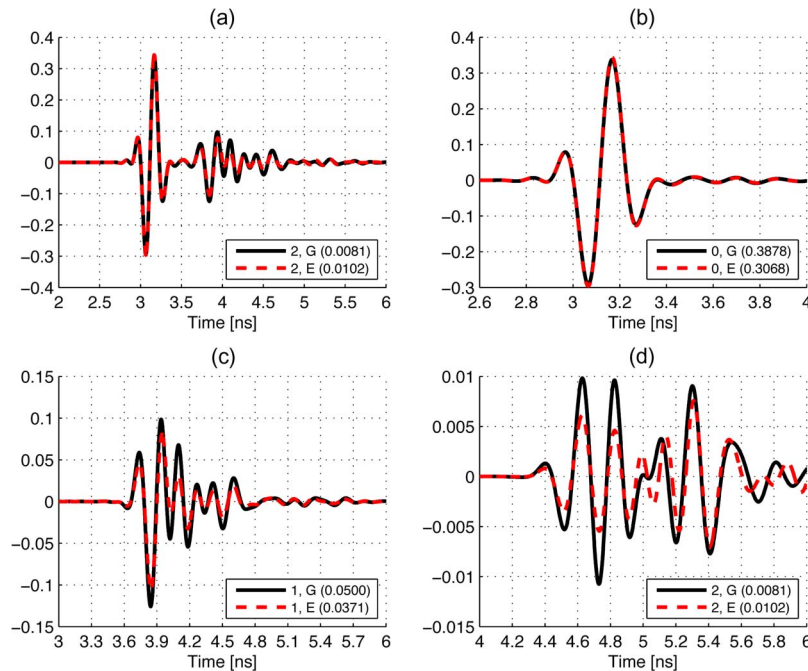


Fig. 12. Time responses s_{sca} of the scattered field computed from GPILE. The parameters are the same as in Fig. 8, and the results obtained from an exponential ACF are also plotted.

with three random rough interfaces separating homogeneous media. It has been applied to simulate the GPR signal over deteriorated pavement structures with embedded interlayer debonding. As a reference, PILE has been used to simulate the GPR signal over the healthy pavement structure

with two rough interfaces only. The comparison between both methods has shown that the GPR signal is sensitive to the embedded debonding ($\lambda_{max}/4$ in thickness) in terms of signal time spread and amplitude variations. Nevertheless, extended simulation with various parameters is required to

test some data processing techniques and to draw some strategy for the detection of the debonding within the pavement structure.

APPENDIX A GENERALIZATION OF THE PILE METHOD TO M INTERFACES

This appendix presents the generalization of the PILE method to M rough interfaces separating homogeneous media.

From the boundary integral equations, the surface currents ψ_i and $\partial\psi_i/\partial n$ on each surface S_i ($i = \{1, 2, \dots, M\}$) must be determined. From the MoM, the boundary integral equations are discretized on each surface of the scatterer, leading to the linear system $\bar{Z}\mathbf{X} = \mathbf{b}$. The unknown vector is then

$$\mathbf{X} = \begin{bmatrix} \mathbf{X}_1 \\ \mathbf{X}_2 \\ \vdots \\ \mathbf{X}_M \end{bmatrix} \quad \mathbf{b} = \begin{bmatrix} \mathbf{b}_1 \\ \mathbf{0} \\ \vdots \\ \mathbf{0} \end{bmatrix} \quad (\text{A1})$$

and the impedance matrix \bar{Z} of size $4(\sum_{i=1}^M N_i)^2$ is expressed as

$$\bar{Z} = \begin{bmatrix} \bar{Z}_1 & \bar{Z}_{21} & \bar{\mathbf{0}} & \bar{\mathbf{0}} & \dots & \bar{\mathbf{0}} & \bar{\mathbf{0}} \\ \bar{Z}_{12} & \bar{Z}_2 & \bar{Z}_{32} & \bar{\mathbf{0}} & \dots & \bar{\mathbf{0}} & \bar{\mathbf{0}} \\ \bar{\mathbf{0}} & \bar{Z}_{23} & \bar{Z}_3 & \bar{Z}_{43} & \dots & \bar{\mathbf{0}} & \bar{\mathbf{0}} \\ \bar{\mathbf{0}} & \bar{\mathbf{0}} & \bar{Z}_{34} & \bar{Z}_4 & \dots & \bar{\mathbf{0}} & \bar{\mathbf{0}} \\ \vdots & \vdots & \vdots & \vdots & \vdots & \vdots & \vdots \\ \bar{\mathbf{0}} & \bar{\mathbf{0}} & \dots & \bar{\mathbf{0}} & \bar{Z}_{M-2,M-1} & \bar{Z}_{M-1} & \bar{Z}_{M,M-1} \\ \bar{\mathbf{0}} & \bar{\mathbf{0}} & \dots & \bar{\mathbf{0}} & \bar{\mathbf{0}} & \bar{Z}_{M-1,M} & \bar{Z}_M \end{bmatrix}. \quad (\text{A2})$$

In addition

$$\mathbf{X}_i = \left[\psi_i(\mathbf{r}_1) \dots \psi_i(\mathbf{r}_{N_i}) \frac{\partial\psi_i(\mathbf{r}_1)}{\partial n} \dots \frac{\partial\psi_i(\mathbf{r}_{N_i})}{\partial n} \right]^T \quad (\text{A3})$$

where $\mathbf{r}_{p \in [1; N_i]} \in S_i$.

We can note that the coupling matrices $\bar{Z}_{i+2,i}$ and $\bar{Z}_{i,i+2}$ vanish because there is no direct interaction between interfaces S_i and S_{i+2} ($i+2 \leq M$).

From (18), the surface currents at the order p_i on the interface i are expressed as

$$\mathbf{Y}_i^{(p_i)} = \bar{Z}_i^{-1} \bar{Z}_{i,i} \sum_{p_{i+1}=0}^{P_{i+1}} \mathbf{Y}_{i+1}^{(p_{i+1})} \quad (\text{A4})$$

where

$$\begin{cases} \mathbf{Y}_{i+1}^{(0)} = \bar{Z}_{i+1}^{-1} \bar{Z}_{i,i+1} \mathbf{Y}_i^{(p_{i+1}-1)} & \text{for } p_{i+1} = 0 \\ \mathbf{Y}_{i+1}^{(p_{i+1})} = \bar{M}_{c,i+1} \mathbf{Y}_{i+1}^{(p_{i+1}-1)} & \text{for } p_{i+1} > 0 \end{cases} \quad (\text{A5})$$

$$\bar{M}_{c,i+1} = \bar{Z}_{i+1}^{-1} \bar{Z}_{i+2,i+1} \bar{Z}_{i+2}^{-1} \bar{Z}_{i+1,i+2} \in [0; M-2]. \quad (\text{A6})$$

Equation (A4) computes the currents $\mathbf{Y}_i^{(p_i)}$ from the currents $\mathbf{Y}_{i+1}^{(p_{i+1})}$ defined on the interface $i+1$ and at the order p_{i+1} .

The order P_{i+1} corresponds to the number of back-and-forth between the interfaces S_i and S_{i+1} which contribute to the scattering process.

To initialize the algorithm, the surface currents $\mathbf{Y}_i^{(0)}$ on the surface $i \in [1; M-1]$ at the zeroth order must be determined. They are expressed as

$$\begin{cases} \mathbf{Y}_1^{(0)} = \bar{Z}_1^{-1} \mathbf{b}_1 & \text{for } i = 1 \\ \mathbf{Y}_{i+1}^{(0)} = \bar{Z}_{i+1}^{-1} \bar{Z}_{i,i+1} \mathbf{Y}_i^{(0)} & \text{for } i > 1. \end{cases} \quad (\text{A7})$$

To start the process, first, the surface currents $\{\mathbf{Y}_{M-1}^{(0)}, \mathbf{Y}_{M-1}^{(1)}, \dots, \mathbf{Y}_{M-1}^{(P_{M-1})}\}$ on the interface $M-1$ are computed from $\mathbf{Y}_{M-2}^{(0)}$. Second, from these surface currents, the surface currents on the interface $M-1$ at the higher orders up to P_{M-2} are computed. These operations are repeated up to interface 1. Then, the total surface currents on interface 1 are

$$\mathbf{X}_1 = \sum_{p_1=0}^{P_1} \mathbf{Y}_1^{(p_1)}. \quad (\text{A8})$$

In addition, the surface currents \mathbf{X}_{i+1} on the interface $i+1$ are related to the surface \mathbf{X}_i on the interface i via

$$\mathbf{X}_{i+1} = -\bar{Z}_{i+1}^{-1} \bar{Z}_{i+1,i} \mathbf{X}_i. \quad (\text{A9})$$

ACKNOWLEDGMENT

The authors would like to thank the anonymous reviewers for their useful comments. This work may contribute to COST Action TU1208 Civil Engineering Applications of Ground Penetrating Radar and to the RILEM Technical Committee 241 on Mechanisms of Cracking and Debonding in Asphalt and Composite Pavements.

REFERENCES

- [1] A. Benedetto, F. Benedetto, M. R. De Blasiis, and G. Giunta, "Reliability of signal processing technique for pavement damages detection and classification using ground penetrating radar," *IEEE Sens. J.*, vol. 5, no. 3, pp. 471–480, Jun. 2005.
- [2] I. L. AL-Qadia and S. Lahouarb, "Measuring layer thicknesses with GPR—Theory to practice," *Construction Build. Mater.*, vol. 19, no. 10, pp. 763–772, Dec. 2005.
- [3] S. Lahouara and I. L. Al-Qadic, "Automatic detection of multiple pavement layers from GPR data," *NDT & E Int.*, vol. 41, no. 2, pp. 69–81, Mar. 2008.
- [4] U. Spagnolini and V. Rampa, "Multitarget detection/tracking for monostatic ground penetrating radar: Application to pavement profiling," *IEEE Trans. Geosci. Remote Sens.*, vol. 37, no. 1, pp. 383–394, Jan. 1999.
- [5] U. Spagnolini, "Permittivity measurements of multilayered media with monostatic pulse radar," *IEEE Trans. Geosci. Remote Sens.*, vol. 35, no. 2, pp. 454–463, Mar. 1997.
- [6] T. Saarenketo and T. Scullion, "Road evaluation with ground penetrating radar," *J. Appl. Geophys.*, vol. 43, no. 2–4, pp. 119–138, Mar. 2000.
- [7] J.-M. Simonin *et al.*, "Detection of debonding and vertical cracks with ND techniques during accelerated tests," in *Proc. 4th Int. Conf. Accelerated Pavement Testing*, Davis, CA, USA, pp. 121–131, Sep. 2012.
- [8] RILEM 241-MCD, Mechanisms of Cracking and Debonding in Asphalt and Composite Pavements, Chair: Pr. W. Buttlar, 2011–2016. [Online]. Available: <http://www.rilem.org/>
- [9] A. Giannopoulos, "Modelling ground penetrating radar by GPRmax," *Construction Build. Mater.*, vol. 19, pp. 755–762, Dec. 2005.
- [10] N. Diamanti and D. Redman, "Field observations and numerical models of GPR response from vertical pavement cracks," *J. Appl. Phys.*, vol. 81, pp. 106–116, Jun. 2012.

- [11] B. Yang and C. Rappaport, "Response of realistic soil for GPR applications with 2-D FDTD," *IEEE Trans. Geosci. Remote Sens.*, vol. 39, no. 6, pp. 1198–1205, Jun. 2001.
- [12] C. Le Bastard, V. Baltazart, Y. Wang, and J. Saillard, "Thin-pavement thickness estimation using GPR with high-resolution and superresolution methods," *IEEE Trans. Geosci. Remote Sens.*, vol. 45, no. 8, pp. 2511–2519, Aug. 2007.
- [13] C. Bourlier, C. Le Bastard, and N. Pinel, "Full wave PILE method for the electromagnetic scattering from random rough layer," *Proc. GPR Int. Conf. Ground Penetrating Radar*, 2014, pp. 545–551.
- [14] N. Déchamps, N. De Beaucoudrey, C. Bourlier, and S. Toutain, "Fast numerical method for electromagnetic scattering by rough layered interfaces: Propagation-inside-layer expansion method," *J. Opt. Soc. Amer. A*, vol. 23, no. 2, pp. 359–369, Feb. 2006.
- [15] C. Bourlier, G. Kubické, and N. Déchamps, "A fast method to compute scattering by a buried object under a randomly rough surface: PILE combined to FB-SA," *J. Opt. Soc. Amer. A*, vol. 25, no. 4, pp. 891–902, Apr. 2008.
- [16] C. Bourlier, N. Pinel, and G. Kubické, *Method of Moments for 2-D Scattering Problems. Basic Concepts and Applications*. Hoboken, NJ, USA: Wiley, 2013, ser. FOCUS SERIES in WAVES.
- [17] N. Pinel, C. Le Bastard, C. Bourlier, and M. Sun, "Asymptotic modeling of coherent scattering from random rough layers: Application to road survey by GPR at nadir," *Int. J. Antennas Propag.*, vol. 2012, pp. 1–9, 2012.
- [18] N. Pinel, C. Le Bastard, V. Baltazart, C. Bourlier, and Y. Wang, "Influence of layer roughness for road survey by ground penetrating radar at nadir: Theoretical study," *IET Radar, Sonar Navig.*, vol. 5, no. 6, pp. 650–656, Jul. 2011.
- [19] F. Koudogbo, P. Combes, and H. J. Mametsa, "Numerical and experimental made rough surfaces," *Progress Electromagn. Res.*, vol. 46, pp. 203–244, 2004.
- [20] E. S. Li and K. Sarabandi, "Low grazing incidence millimeterwave scattering models and measurements for various road surfaces," *IEEE Trans. Antennas Propag.*, vol. 47, no. 5, pp. 851–861, May 1999.



Cédric Le Bastard received the B.S. and M.S. degrees in electronic engineering from the University of Rennes, Rennes, France, in 2001 and 2003, respectively, and the Ph.D. degree from the Central des Ponts et Chaussées Laboratory, University of Nantes, Nantes, France, in 2007.

He is currently with the Centre for Expertise and Engineering on Risks, Environment, Mobility, Urban and Country Planning (Cerema) and is also an Associate Researcher with the Institute of Electronics and Telecommunications of Rennes, France (IETR). His

research interests include radar, nondestructive testing and evaluation, electromagnetic wave scattering, time-delay estimation, and array signal processing.



Vincent Baltazart received the Ph.D. degree in signal processing from the University of Rennes, Rennes, France, in 1994.

From 1992 to 1993, he worked on ionospheric modeling and propagation at IPS Radio and Space Services, Sydney, Australia. From 1994 to 1996, he worked on microwave remote-sensing techniques at the Université Catholique de Louvain, Louvain-la-Neuve, Belgium. In 1996, he joined the Laboratoire Central des Ponts et Chaussées, France, as a researcher in the field of optical sensors. He is

currently involved in nondestructive testing and evaluation techniques for civil engineering applications at IFSTTAR in Nantes.



Christophe Bourlier was born in La Flèche, France, on July 6, 1971. He received the M.S. degree in electronics from the University of Rennes, Rennes, France, in 1995 and the Ph.D. degree from the Système Électronique et Informatique (SEI) Laboratory, Nantes, France, in 1999.

He is currently with the Institute of Electronics and Telecommunications of Rennes, France (IETR) Laboratory, Polytech Nantes (University of Nantes), Nantes, France. He is a Researcher with the National Center for Scientific Research, working on electro-

magnetic wave scattering from rough surfaces (ocean-like surfaces) and objects for microwaves and infrared remote sensing applications and radar signatures. He is the author of more than 180 journal articles and conference papers.